

Submitted to ApJ

The Host Galaxy of the Lensed Quasar Q 0957+561¹

C. R. Keeton^(a),

E. E. Falco^(b), C. D. Impey^(a), C. S. Kochanek^(b), J. Lehár^(b), B. A. McLeod^(b),

H.-W. Rix^(c), J. A. Muñoz^(b), and C. Y. Peng^(a)

^(a)Steward Observatory, University of Arizona, Tucson, AZ 85721

email: ckeeton, cimpey, cyp@as.arizona.edu

^(b)Harvard-Smithsonian Center for Astrophysics, 60 Garden St., Cambridge, MA 02138

email: efalco, ckochanek, jlehar, bmcleod, jmunoz@cfa.harvard.edu

^(c)Max-Planck-Institut für Astronomie, Koenigsstuhl 17, D-69117 Heidelberg, Germany

email: rix@mpia-hd.mpg.de

ABSTRACT

Infrared images of the Q 0957+561 gravitational lens obtained with the Hubble Space Telescope show two large ($\sim 5''$) lensed images of the $z_s = 1.41$ quasar host galaxy. Parts of the host galaxy are doubly-imaged like the quasar, while other parts are quadruply-imaged. The distortions of the host galaxy offer the best probe yet of the global structure of the lensing potential, which is essential for determining the Hubble constant from the measured time delay. The distortions are inconsistent with the predictions of previously published lens models, which invalidates those models and their implications for H_0 . New models show that the distortions finally break the long-standing degeneracy between the shape of the lens galaxy and the tidal shear contributed by the cluster containing the lens galaxy. The shape of the lens galaxy's mass distribution must be remarkably similar to the shape of its luminosity distribution, and most models that produce reasonable values for the Hubble constant roughly match the observed ellipticity gradient and isophote twist of the lens galaxy. Also, the cluster must be non-spherical and produce a relatively small tidal shear. Although there are still degeneracies in the lens models that lead to a 25% uncertainty in the derived value of the Hubble constant, there are also strong prospects for new observations to further improve the constraints and reduce the uncertainties.

¹Based on Observations made with the NASA/ESA Hubble Space Telescope, obtained at the Space Telescope Science Institute, which is operated by AURA, Inc., under NASA contract NAS 5-26555.

1. Introduction

Gravitational lenses offer an attractive independent method of determining the Hubble constant (H_0) on cosmological scales without the systematic difficulties associated with the local distance ladder (Refsdal 1964, 1966). Six of the more than 50 known gravitational lenses now have time delays that can be used to estimate H_0 : B 0218+357 (Biggs et al. 1999); Q 0957+561 (Schild & Thomson 1995; Kundić et al. 1997; Haarsma et al. 1999); PG 1115+080 (Schechter et al. 1997; Barkana 1997); B 1600+434 (Hjorth et al. 1999); B 1608+656 (Fassnacht et al. 1999); and PKS 1830–211 (Lovell et al. 1998); preliminary H_0 estimates for five of these systems have been compiled by Koopmans & Fassnacht (1999). Once a time delay is accurately determined, the uncertainties in the derived value of the Hubble constant are due almost entirely to the systematic uncertainties in the model for the lensing potential, plus “cosmic variance” due to the effects of weak density inhomogeneities along the line of sight (Seljak 1994; Barkana 1996).

Only two of the time delay lenses have been modeled in sufficient detail to fully understand the systematic uncertainties created by their geometries: Q 0957+561 (Falco, Gorenstein & Shapiro 1985, 1991; Kochanek 1991; Bernstein, Tyson & Kochanek 1993; Grogin & Narayan 1996; Chartas et al. 1998; Barkana et al. 1999; Bernstein & Fischer 1999; Chae 1999; Romanowsky & Kochanek 1999), and PG 1115+080 (Schechter et al. 1997; Courbin et al. 1997; Keeton & Kochanek 1997; Saha & Williams 1997; Impey et al. 1998). In Q 0957+561, the lens consists of a brightest cluster galaxy and its parent cluster, and the value of the Hubble constant depends on the mass balance between the two components. Judgments about the ability of models to determine the correct mass balance vary significantly: optimistic estimates yield $H_0 = 61^{+13}_{-15}$ km s $^{-1}$ Mpc $^{-1}$ at 95% confidence (Grogin & Narayan 1996, using the stellar dynamical models of Romanowsky & Kochanek 1999); while more pessimistic estimates yield $H_0 = 77^{+29}_{-24}$ (Kochanek 1991; Bernstein et al. 1993; Bernstein & Fischer 1999). In PG 1115+080, the lens is one of the brighter galaxies in a small group, but the four-image geometry easily determines the relative roles of the primary lens galaxy and the group. Instead, the value of the Hubble constant depends on the assumed radial mass distribution of the primary lens galaxy. Galaxy models with dark matter and mass distributions consistent with the best estimates for early-type galaxies lead to low values for the Hubble constant ($H_0 = 44 \pm 4$ km s $^{-1}$ Mpc $^{-1}$; Impey et al. 1998).

Impey et al. (1998) discovered an Einstein ring image of the quasar host galaxy in the PG 1115+080 lens, and noted that the geometry of the ring could be used to break the degeneracy in the lens models. Here we report the discovery of the host galaxy in the Q 0957+561 lens and discuss the implications for lens models and the Hubble constant. In §2 we describe our observations. In §3 we discuss the data and methods used to model the system, summarizing previous work and introducing our new data and techniques. In §4 we examine the arcs predicted by previously published lens models and demonstrate that they fail to match the observed arcs. In §5 we present new models that match all data, including the arcs, and discuss their implications for the properties of the lens galaxy and cluster and for H_0 . In §6 we summarize our results and discuss prospects for further improving the constraints on this lens system and on H_0 .

2. Observations

We observed Q 0957+561 with the Hubble Space Telescope as part of the CfA–Arizona Space Telescope Lens Survey (CASTLES; Lehár et al. 1999; Falco et al. 1999). Using the NIC2 camera, we obtained a 2800-second F160W (H band) image of Q 0957+561 divided into four dithered exposures. A log of the observations is presented in Table 1. We reduced the images using `nicred`, a custom reduction package developed for CASTLES (Lehár et al. 1999). We also reanalyzed archival WFPC2 images, including a 32200-second F555W (V band) exposure and a 2620-second F814W (I band) exposure (Bernstein et al. 1997). In the optical images, Q 0957+561 fell in chip WF3 of the WFPC2 camera (with pixel size $\sim 0''.1$, compared to $\sim 0''.076$ for NIC2). Because the images A and B of Q 0957+561 were saturated in the WFPC2 images, we derived our astrometry of A, B and the lens galaxy G1 exclusively from our unsaturated NIC2 data.

Figure 1a shows our combined H band image, which prominently shows the lens galaxy and the two quasar images. The quasar host galaxy is visible as a faint arc next to the quasar A image. Table 2 summarizes a photometric model consisting of point sources for the two quasar images and elliptical de Vaucouleurs models for the main lens galaxy (G1) and a neighboring galaxy (G2, not seen in Figure 1).² The lens galaxy is known to have a small ellipticity gradient and isophote twist (Bernstein et al. 1997), but we used only a simple elliptical model. Figure 1b shows the residuals after subtracting the PSF-convolved photometric model from the original image, and Figure 1c shows these residuals convolved with a $\sim 0''.076$ (1 pixel) FWHM Gaussian to enhance the visibility of low surface brightness features. The residual image shows the host galaxy image near quasar A to be an arc distorted tangentially relative to the lens galaxy. It also reveals an extended asymmetric arc near the B quasar image. If the residuals near quasar B were created by the error of fitting a simple elliptical surface brightness model to a galaxy with a radially varying ellipticity and orientation, we would expect them to have reflection symmetry through the center of the galaxy. Because the arc near quasar B lacks such symmetry, we conclude that it is the lensed counterpart of the arc near quasar A, and that both are images of the quasar host galaxy.

The residual H band image also shows two additional sources, one east of quasar A and another just west of quasar B (labeled G3 and G4 in Figure 1c). Their positions and photometric properties are given in Table 2. These objects correspond in position and V magnitude to two of the faint sources seen in the deep V band image and labeled Blobs 7 and 1 (respectively) by Bernstein et al. (1997). Their colors (especially V–I) are similar to those of G1 and G2 and suggest that they are probably faint cluster members. Whether or not they are associated with the cluster, it is clear that they are not multiply imaged and are not associated with the quasar source. The fact that G4 is not part of the host galaxy arc will be important to remember when examining the arc structure

²Young et al. (1981) tabulated objects in the field of Q 0957+561 and applied the labels G1–G5 to five of the bright galaxies. We labeled only objects close to the lens galaxy, so other than G1 our labels do not match those of Young et al. Our object G2 appears as object #97 in their Table 1. Our objects G3 and G4 do not appear in their list.

predicted by lens models (see §3.3).

The lensed host galaxy is not detected at significant levels in the shallow I band image, although a visual examination suggests that low-level residuals are present and should be detected at a significant level with a longer integration. The deep V band image does not have large extended arcs, but it does show seven faint “blobs” and a thin arclet (Bernstein et al. 1997). As noted above, at least two of the blobs are probably faint cluster galaxies. However, Blobs 2 and 3 and the arclet have been identified as possible lensed features, and lens models support this interpretation (Barkana et al. 1999; Bernstein & Fischer 1999; Chae 1999). Since the V band corresponds to rest-frame UV at the quasar redshift $z_s = 1.41$, these features probably correspond to discrete star forming regions in the host galaxy. We follow previous models and include Blobs 2 and 3 plus two “Knots” in the arclet as model constraints (see §3.2).

We estimated the fluxes of the host galaxy images using the IRAF task `polyphot`, which measures fluxes within polygonal apertures. We traced polygonal apertures along the edges of the distorted images of the host galaxy at the 3σ level above the sky. We found that both lensed images of the host galaxy have H band brightnesses of ~ 18.4 mag, and a surface brightness of ~ 20.6 mag/arcsec 2 (both images have approximately the same area). The main source of uncertainty for the brightness estimates is the relatively large size of the residuals from the subtraction of the quasar images, compared to the (low) brightness levels of the arcs; we estimate the uncertainties to be ~ 0.3 mag.

Given an acceptable lens model we can map the host galaxy images to the source plane to obtain a map of the unlensed host galaxy (see §3.3). In principle we could use the source maps to measure the photometric properties of the host galaxy. However, in practice the imperfect quasar subtraction corrupts the flux in the bright central regions of the source and hinders the measurement. One robust statement we can make is that part of the host galaxy is doubly-imaged like the quasar, but part of it is quadruply-imaged (see §4). This accounts for the shape differences between the A and B arcs: the A arc is a single distorted image of the host galaxy, while the B arc is a composite of three images that straddle the lensing critical line.

3. Constraining models of Q 0957+561

Q 0957+561 is the most thoroughly studied gravitational lens. The system comprises a radio-loud quasar at redshift $z_s = 1.41$ lensed into two images by a brightest cluster galaxy and its parent cluster at redshift $z_l = 0.36$ (Walsh, Carswell & Weymann 1979; Young et al. 1980). There is a time delay of 417 ± 3 days between the images (Schild & Thomson 1995; Kundić et al. 1997; Haarsma et al. 1999). VLBI observations have resolved each image into a core and ~ 80 milli-arcsecond jet (Garrett et al. 1994). Deep optical images have uncovered faint “Blobs” and “Knots” that are probably lensed image pairs of star forming regions in the quasar host galaxy (Bernstein et al. 1997). Our observations have revealed infrared arcs representing distorted images of the quasar

host galaxy. In this section we discuss how to use these and other data to constrain models of the system and values for the Hubble constant H_0 . In §3.1 we review the theory of lens modeling and discuss important model degeneracies. In §§3.2 and 3.3 we discuss previous and new observational constraints on models. In §§3.4 and 3.5 we describe classes of models applied to the lens galaxy and cluster in Q 0957+561, summarizing previous classes and introducing a new one. Finally, in §3.6 we discuss how we apply the observational constraints to our new class of models.

3.1. Basic lens theory: model degeneracies

In a multiply-imaged gravitational lens system, the light from a distant source is deflected by the gravitational potential of foreground objects so that we observe multiple images of the source. The lensing potential is usually dominated by a single galaxy, although there may be non-negligible perturbations from other objects nearby.³ Basic lens theory is presented in the book by Schneider, Ehlers & Falco (1992), and we quote the relevant results here. The lensing potential ϕ is determined by the two-dimensional Poisson equation $\nabla^2\phi = 2\kappa$, where $\kappa = \Sigma/\Sigma_{crit}$ is the surface mass density in units of the critical surface density for lensing (in angular units),

$$\Sigma_{crit} = \frac{c^2}{4\pi G} \frac{D_{ol}D_{os}}{D_{ls}} , \quad (1)$$

where D_{ol} and D_{os} are angular diameter distances from the observer to the lens and source, respectively, and D_{ls} is the angular diameter distance from the lens to the source. The lensing potential deflects a light ray so that the angular position \vec{u} of the source on the sky and the angular position \vec{x} of an image are related by the lens equation,

$$\vec{u} = \vec{x} - \vec{\nabla}\phi(\vec{x}) . \quad (2)$$

There is an image corresponding to each solution \vec{x}_i of this equation. Lensing introduces a time delay between the ray paths of two images of the same source. The time delay between images at positions \vec{x}_i and \vec{x}_j is

$$\Delta t_{ij} = \frac{1+z_l}{c} \frac{D_{ol}D_{os}}{D_{ls}} \left[\frac{1}{2} \left(|\vec{x}_i - \vec{u}|^2 - |\vec{x}_j - \vec{u}|^2 \right) - \left(\phi(\vec{x}_i) - \phi(\vec{x}_j) \right) \right] , \quad (3)$$

where z_l is the redshift of the lens. This equation is the basis of attempts to use lensing to determine the Hubble constant H_0 . By measuring light curves of images one can determine the time delay Δt_{ij} . A lens model gives the term in square brackets in eq. (3). The combination of distances is $\propto H_0^{-1}$ and only weakly dependent on other cosmological parameters.

³There may also be a contribution to the potential from density fluctuations along the line of sight, but it is usually small compared to the contribution from objects at the same redshift as the main lens galaxy (Seljak 1994; Barkana 1996; Keeton, Kochanek & Seljak 1997). In a few cases there are two lens galaxies enclosed by the lensed images (e.g. Jackson, Nair & Browne 1997; Koopmans et al. 1999), but this complication is not an issue in Q 0957+561.

A lens model consists of a description of the lensing potential ϕ . The observed images provide two principle constraints on such a model. First, roughly speaking an image at projected distance R from the main lens galaxy measures the enclosed mass $M(R)$. In Q 0957+561 and many 2-image gravitational lenses, the two images lie at different distances $R_1 \neq R_2$, so they measure two masses $M(R_1)$ and $M(R_2)$ and hence constrain the mass profile (e.g. Grogin & Narayan 1996). Second, with at least three well-determined positions (two images and the lens galaxy, or four images), the images determine the quadrupole moment of the net potential. However, there are four properties of the mass distribution that must be determined for a complete description of the model: the mass profile of the main lens galaxy; the shape (ellipticity and orientation) of the main lens galaxy; the shear from the the gravitational tidal field induced by objects near the lens galaxy; and the amount of gravitational focusing (or “convergence”) contributed by the environment of the lens galaxy.

With more unknown quantities than constraints, there are two common degeneracies in the lens models. First, to lowest order the convergence κ contributed by the environment cannot be determined by lens models, which leads to the so-called “mass sheet degeneracy” (Falco et al. 1985). If a lensing potential $\phi(\vec{x})$ fits the observed data, then any potential

$$\phi'(\vec{x}) = \frac{1}{2} \kappa |\vec{x}|^2 + (1 - \kappa) \phi(x) \quad (4)$$

will fit the data equally well. The κ term is equivalent to the potential from a uniform mass sheet with surface density $\Sigma = \kappa \Sigma_{crit}$. The only potentially observable difference between the lens models represented by ϕ and ϕ' is in the predicted time delays,

$$\Delta t'_{model} = (1 - \kappa) \Delta t_{model}. \quad (5)$$

However, this effect is not observable if we want to use gravitational lensing to determine the Hubble constant because it simply translates into a scaling of the inferred value for H_0 . If H_0 and H'_0 are the values inferred from the two lens models, then

$$H'_0 = (1 - \kappa) H_0. \quad (6)$$

This analysis has used only the lowest order term of the contribution from the environment, but the higher order terms cannot necessarily eliminate the degeneracy (e.g. Chae 1999). The mass sheet degeneracy is important for Q 0957+561 because the parent cluster of the lens galaxy contributes a significant convergence. The only way to break this degeneracy is to obtain an independent mass constraint to determine the relative contributions of the main lens galaxy and the environment to the mass enclosed by the images (see §3.2).

The second important degeneracy is between the shape of the main lens galaxy and the shear from the gravitational tidal field of objects in the environment of the lens galaxy. Because the images determine only the quadrupole moment of the total potential, there can be a wide range of parameter space in which the lens galaxy ellipticity and the external shear combine to produce the required joint quadrupole (e.g. Keeton et al. 1997). Consider a 2-image lens with image positions

\vec{x}_A and \vec{x}_B , a galaxy potential ϕ_{gal} , and an external shear with amplitude γ and direction θ_γ . Fitting the image positions exactly is equivalent to solving the equation

$$\vec{x}_A - \vec{\nabla}\phi_{gal}(\vec{x}_A) - \Gamma \cdot \vec{x}_A = \vec{x}_B - \vec{\nabla}\phi_{gal}(\vec{x}_B) - \Gamma \cdot \vec{x}_B \quad (7)$$

where the shear is described by the tensor

$$\Gamma = \begin{bmatrix} \gamma \cos 2\theta_\gamma & \gamma \sin 2\theta_\gamma \\ \gamma \sin 2\theta_\gamma & -\gamma \cos 2\theta_\gamma \end{bmatrix}. \quad (8)$$

No matter what galaxy potential ϕ_{gal} is used, it is straightforward to solve eq. (7) for the shear parameters γ and θ_γ . In other words, one can fit the image positions in a 2-image lens to arbitrary precision for *any model lens galaxy*, although in some cases the inferred shear γ may be unphysically strong.

Constraints from the images fluxes or additional images often break this degeneracy, although the 1σ range of models may still be large. In previous models of Q 0957+561, the additional constraints came primarily from the VLBI observations of the quasar images, which show several discrete components with ~ 0.1 milli-arcsecond errorbars (Garrett et al. 1994; Barkana et al. 1999). It is easy to be misled about the true structure of the potential, however, when using such strong constraints (see Kochanek 1991; Bernstein et al. 1993; Bernstein & Fischer 1999). Internal structure in the lens galaxy, such as isophote twists or lumpiness in the mass distribution, may affect the images at sub-milli-arcsecond scales (e.g. Mao & Schneider 1998). Neglecting that structure forces the models to adjust large-scale model components in order to fit small-scale constraints, leading them to converge to a best-fit solution that is well defined (i.e. with no apparent degeneracy) but incorrect. In Q 0957+561, the observed ellipticity gradient and isophote twist suggest that the galaxy does have important internal structure (Bernstein & Fischer 1997), and in §4 we show that models neglecting this structure indeed converged to incorrect solutions.

3.2. Previous observational constraints

In Q 0957+561 the high-resolution VLBI maps of the quasar images provide strong position constraints, plus somewhat weaker constraints on the relative magnification matrix between the images (Garrett et al. 1994; Barkana et al. 1999). The optical Blobs and Knots offer additional but weaker position constraints. The Knots are particularly useful because they appear to represent a pair of “fold” images and thus require the lensing critical line to pass between them (see Bernstein & Fischer 1999). The constraints from these images leave two of the three model degeneracies discussed in §3.1: the mass sheet degeneracy due to the convergence provided by the cluster; and the degeneracy between the lens galaxy shape and the cluster shear.

Several steps have been taken to break the mass sheet degeneracy by determining the relative masses of the lens galaxy and cluster. First, Rhee (1991), Falco et al. (1997), and Tonry & Franx

(1999) measured the lens galaxy’s central velocity dispersion to be $288 \pm 9 \text{ km s}^{-1}$. Romanowsky & Kochanek (1999) used stellar dynamical models to translate this into constraints on the lens galaxy mass and concluded that $(80 \pm 12)\%$ of the image separation is contributed by the galaxy (and the rest by the cluster convergence). Second, Fischer et al. (1997) detected a weak lensing signal from the cluster, which Bernstein & Fischer (1999) translated into an estimate of the mean surface density of all mass inside an aperture of radius $30''$ centered on the lens galaxy,

$$\langle \kappa_{obs} \rangle_{30''} = \langle \Sigma \rangle_{30''} / \Sigma_{crit} = 0.26 \pm 0.08. \quad (9)$$

Furthermore, Bernstein & Fischer (1999) showed that the surface mass density $\kappa_{clus} = \Sigma_{clus} / \Sigma_{crit}$ of the cluster at the position of the lens galaxy is given by

$$1 - \kappa_{clus} = \frac{1 - \langle \kappa_{obs} \rangle_{30''}}{1 - \langle \kappa_{mod} \rangle_{30''}}, \quad (10)$$

where $\langle \kappa_{mod} \rangle$ is the mean mass density of a model lens galaxy. In this way one can combine the weak lensing measurement with a lens model to estimate κ_{clus} (see §5.3). There have been other attempts to measure the cluster mass, using the velocity dispersion of the galaxies in the cluster ($715 \pm 130 \text{ km s}^{-1}$; Garrett, Walsh & Carswell 1992; Angonin-Willaime, Soucail & Vanderriest 1994) or the X-rays from the cluster gas (Chartas et al. 1998), but they are still limited by significant systematic uncertainties.

Although measurements of the cluster surface density are important (especially for determining H_0 , see §5.4), they do not break the degeneracy between the lens galaxy shape and the cluster shear. Another approach is to constrain the shape of the lens galaxy’s mass distribution. The orientation of the lens galaxy’s light distribution should offer a guide to the orientation of its mass distribution, because other lenses suggest that mass and light are at least roughly aligned (typically within $\sim 10^\circ$; Keeton, Kochanek & Falco 1998). An important detail, though, is that the lens galaxy has a radially varying ellipticity and orientation (Bernstein et al. 1997): the ellipticity increases from ~ 0.1 inside a radius of $1''$ to ~ 0.4 outside $10''$, and the PA varies from $\sim 40^\circ$ to $\sim 60^\circ$ (albeit with large uncertainties). These variations suggest that the galaxy’s projected mass distribution may not have simple elliptical symmetry, and they may well need to be incorporated into lens models.

3.3. New constraints from the host galaxy arcs

The host galaxy arcs act as an extensive set of position constraints that may break the degeneracy between the lens galaxy shape and the cluster shear. Although the intrinsic source structure is unknown, the simplicity of the lensing geometry means that we can model the arcs self-consistently using a modified version of the Ring Cycle algorithm of Kochanek et al. (1989). Specifically, we know that there is a one-to-one mapping between the A image of the host galaxy and the source, so for a given lens model we can project the A arc back to the source plane to obtain the correct

source structure for that lens model.⁴ We can then reproject that source onto the image plane to predict the structure of the B arc. Since the arcs are very large compared to the size of the PSF, there is no need to include the effects of the PSF. For the arc map we use the smoothed residual image (Figure 1c).

This technique produces maps of the model arcs that can be compared visually to the observed arcs (see Figures 2–4 below). However, for modeling we want to quantify the differences, so we define a χ^2 term for the arcs using a pixel-by-pixel comparison of the observed and model surface brightnesses,

$$\chi_{arc}^2 = \sum_{i=1}^{N_{arc}} \frac{(f_{obs,i} - f_{mod,i})^2}{2\sigma_{sky}^2}. \quad (11)$$

The factor of 2 in the denominator enters because the source is constructed from arc A, so it and the observed B arc each have errorbars of σ_{sky} . To compute χ_{arc}^2 we mask the arc map and use only the region near the B arc, omitting regions near the B quasar and the core of the lens galaxy where imperfect subtraction makes the residual flux unreliable. We also omit the region around the object G4 where the flux is not due to the quasar host galaxy (see §2). The masked region is shown in Figure 1c. To count the number of arc constraints, we count the number of pixels inside the mask for which either the observed arc or the model arc is more than 2σ above the sky and take this to be the number of arc constraints N_{arc} . Typically $N_{arc} \sim 10^4$. Because the source is fully determined from the A arc, we quote $\bar{\chi}_{arc}^2 \equiv \chi_{arc}^2/N_{arc}$ as an effective χ^2/DOF for the arc. The fact that our best models produce $\bar{\chi}_{arc}^2 \simeq 1$ (see §5) suggests that this is a reasonable counting of the constraints.

3.4. Lens galaxy models

Q 0957+561 has been modeled extensively; we summarize results from the recent models by Grogan & Narayan (1996), Barkana et al. (1999), Bernstein & Fischer (1999), and Chae (1999) in Table 3. (Technical details of comparing the models are discussed in Appendix A.) The models fall into two main families based on how they treat the main lens galaxy. First is the “power law” family, in which the lens galaxy is modeled with a circular or elliptical surface density with a softened power law profile: $\Sigma \propto (s^2 + m^2)^{\alpha/2-1}$, where m is an ellipsoidal coordinate, s is a core radius, and α is the power law exponent such that $M(R) \sim R^\alpha$ asymptotically. The best-fit models typically have a small core radius and a power law $\alpha \simeq 1.1$ corresponding to a profile slightly shallower than isothermal. In the second family, called “FGS” models after being introduced by Falco, Gorenstein & Shapiro (1991), the lens galaxy is treated as a circular or elliptical King model, plus a central point mass to account for a mass deficit in the core of the King model.

⁴A similar projection fails for the B arc because in all reasonable models this arc crosses the lensing critical line (see §4). Thus the map from the B arc to the source is not one-to-one.

In almost all of the previous models the lens galaxy was assumed to have a projected mass distribution with circular or elliptical symmetry. However, as discussed in §§3.1 and 3.2 the observed ellipticity gradient and isophote twist suggest that this assumption may not be correct. The key improvement in the models is the addition of internal structure in the lens galaxy’s mass comparable to that seen in its light. While we do not expect the mass to trace the light exactly, it should be given the same freedoms in order to avoid oversimplifying the models.

Bernstein & Fischer (1999) did add freedom to the galaxy’s radial and angular structure by using independent power laws in different radial zones, but this led to unphysical models with density discontinuities that cannot match normal rotation curves. We introduce models that allow similar radial and angular freedom while keeping the density smooth. We start with the pseudo-Jaffe ellipsoid, whose projected density distribution has elliptical symmetry and a profile that is roughly flat inside a core radius s , falls as $\Sigma \propto R^{-1}$ out to a cut-off radius a (yielding a rotation curve that is approximately flat), and then falls as $\Sigma \propto R^{-3}$ to maintain a finite mass; a detailed definition is given in Appendix B. We then construct “double pseudo-Jaffe” models comprising two concentric pseudo-Jaffe components with different scale lengths, ellipticities, and orientations. We fix the model galaxy to its observed position, which leaves 10 galaxy parameters: a mass parameter (b_i), ellipticity (e_i), orientation angle (PA_i), core radius (s_i), and cut-off radius (a_i) for each component ($i = 1, 2$).

The double pseudo-Jaffe model provides a great deal of freedom in the lens galaxy. First, it is essentially a smooth generalization of both the power law and the FGS models. When the inner pseudo-Jaffe component is compact, it mimics the point mass in FGS models while the outer component is similar to the King model (see Appendix B); and when the cut-off radius of the inner component is comparable to the core radius of the outer component, the two components combine to produce nearly a smooth $\alpha = 1$ power law. Second, with this model we can mimic the observed internal structure of the lens galaxy: by adjusting the ellipticities and orientations we can produce a smooth ellipticity gradient and isophote twist. An important difference from the broken power law models of Bernstein & Fischer (1999) is that the double pseudo-Jaffe models have smooth density profiles. We discuss the physical properties of sample double pseudo-Jaffe models in §5.3.

3.5. Cluster models

Previous models have used several different methods for including the cluster’s contribution to the lensing potential. The simplest approach is to expand the cluster potential in a Taylor series and keep only the lowest significant (2nd order) term, which describes the tidal shear produced by the cluster. However, this approximation is thought to be poor for Q 0957+561 because the cluster is close to the lens and the VLBI errorbars are small, so the 3rd order terms are larger than the errorbars. Barkana et al. (1999) and Chae (1999) included all the higher order terms implicitly by introducing a mass distribution to represent the cluster, but degeneracies related to the cluster shape and density profile forced them to make assumptions about the cluster properties. Kochanek

(1991) and Bernstein & Fischer (1999) instead used a Taylor series with general 3rd order terms,

$$\phi_{clus} = \frac{1}{2} \kappa_{clus} r^2 + \frac{1}{2} \gamma r^2 \cos 2(\theta - \theta_\gamma) + \frac{1}{4} \sigma r^3 \sin(\theta - \theta_\sigma) - \frac{1}{6} \delta r^3 \sin 3(\theta - \theta_\delta). \quad (12)$$

The 2nd order κ_{clus} term produces the mass sheet degeneracy, so it is usually omitted from the lens models and constrained independently (see §§3.1 and 3.2). The 2nd order γ term represents the tidal shear from the cluster. The 3rd order σ and δ terms arise from the gradient of the cluster density and the $m = 3$ component of the cluster mass (in a frame centered on the lens galaxy; see Bernstein & Fischer 1999; Keeton 2000). The three direction angles $(\theta_\gamma, \theta_\sigma, \theta_\delta)$ are written here as position angles (i.e. measured East of North).

We follow Bernstein & Fischer (1999) and use the 3rd order Taylor series (omitting the κ_{clus} term). Although we simply fit for the Taylor series parameters, it is important to understand how they relate to physical properties of the cluster and what their reasonable ranges are. In popular cluster mass models the cluster amplitudes (γ, σ, δ) and direction angles $(\theta_\gamma, \theta_\sigma, \theta_\delta)$ have the following properties (Keeton 2000):

- Circularly symmetric mass distribution: the three angles all point to the center of the cluster.
- Singular isothermal ellipsoid: the shear angle θ_γ points to the cluster center and the shear amplitude equals the convergence from the cluster, $\gamma = \kappa_{clus}$. Both of these results hold for all positions and all values of the axis ratio q . The gradient amplitude σ is bounded by $1 \leq \frac{\sigma r_0}{\kappa_{clus}} \leq \frac{1+q^2}{2q}$, where r_0 is the distance from the lens galaxy to the cluster.
- Softened isothermal ellipsoid: Outside of the core the results for the singular isothermal ellipsoid are approximately true. For example, for clusters with an axis ratio $q > 0.6$ the shear angle θ_γ points to within 10° of the cluster center for $r_0 \gtrsim 2s$, where s is the core radius. The cluster has $\kappa_{clus} \geq \gamma$, but $\kappa_{clus} > 2\gamma$ only for $r_0 \lesssim 3s$.
- An ellipsoid with the “universal” dark matter profile of Navarro, Frenk & White (1996): For clusters with an axis ratio $q > 0.6$, the shear angle θ_γ points to within 4° of the cluster center for $r_0 \gtrsim 0.5r_s$, where r_s is the scale radius in the “universal” profile. The cluster generally has $\kappa_{clus} \gtrsim \gamma$ for $r_0 \gtrsim r_s$ and $\kappa_{clus} \lesssim \gamma$ for $r_0 \lesssim r_s$.

We let the shear and gradient parameters $(\gamma, \theta_\gamma, \sigma, \theta_\sigma)$ vary freely, but we keep these general relations in mind when interpreting the results. To avoid an explosion of parameters, we follow Bernstein & Fischer (1999) and use a “restricted” 3rd order cluster with $\theta_\delta = \theta_\sigma$ and $\delta = -3\sigma/2$ (as for a singular isothermal sphere). This model is useful because it requires only four parameters for the cluster, and it can provide model-independent evidence for a non-circular cluster if $\theta_\sigma \neq \theta_\gamma$. We also experimented with models using a singular isothermal mass distribution for the cluster, and we discuss these models briefly but do not quote detailed results (§5).

3.6. Constraining the new models

Our models have 10 galaxy and 4 cluster parameters, but fortunately we need not examine all of them explicitly. First, the general features of the lens allow us to fix two scale radii. The lack of a central image requires that the galaxy be nearly singular, so we set the core radius of the inner pseudo-Jaffe component (s_1) to zero. Also, previous lens models suggest that the galaxy needs to have mass extending at least to the distant A image (5'' from the galaxy), so the cut-off radius of the outer pseudo-Jaffe component (a_2) should be larger than 5''. The model should not be very sensitive to any particular value larger than this, so we fix $a_2 = 30''$ (similar to Bernstein & Fischer 1999).

Second, we can use linear techniques for the two galaxy mass parameters (b_1 and b_2) and the two cluster amplitudes (γ and σ) because they enter the potential as simple multiplicative factors. (This is a variant of solving for the shear parameters in eq. 7.) If we take the strong VLBI constraints on the quasar core and jet positions to be exact (see Kochanek 1991; Bernstein & Fischer 1999), they lead to four linear constraint equations:

$$\text{cores : } \vec{x}_{A1} - \nabla\phi(\vec{x}_{A1}) = \vec{x}_{B1} - \nabla\phi(\vec{x}_{B1}) \quad (13)$$

$$\text{jets : } \vec{x}_{A5} - \nabla\phi(\vec{x}_{A5}) = \vec{x}_{B5} - \nabla\phi(\vec{x}_{B5}) \quad (14)$$

where A_1 and B_1 denote the two quasar cores while A_5 and B_5 denote the brightest jet components; the positions are given by Barkana et al. (1999). The four constraint equations can be solved explicitly to write the four linear parameters as functions of the remaining (non-linear) parameters. This technique ensures that the VLBI constraints are fitted exactly, while reducing by four the number of parameters that must be examined directly.

We are left with 8 explicit parameters: the ellipticities e_1 and e_2 , orientation angles PA_1 and PA_2 , and scale lengths a_1 and s_2 of the galaxy; and the direction angles θ_γ and θ_σ of the cluster. We evaluate models in this parameter space using the remaining constraints: the flux ratios of the quasar cores and jets and the positions of the optical Blobs and Knots (taken from Bernstein & Fischer 1999), and the structure of the arcs (see §3.3). Techniques and results for our new models are discussed in §5.

4. The failure of existing lens models

Previous models of Q 0957+561 (summarized in Table 3) posited that the VLBI observations and the optical Blobs and Knots provided strong enough constraints to break the degeneracy between the lens galaxy shape and the cluster shear. As we discussed in §3.1, however, it is dangerous to use smooth circular or elliptical lens models with high-precision constraints, because the oversimplified models may be forced to converge on a best-fit solution with the wrong global structure for the potential. Until now we have lacked the constraints to test this concern, although

the fact that previous models gave wildly difference shapes for the lens galaxy certainly suggests that the models were not robust.

The host galaxy arcs finally provide an extensive set of constraints for testing the previous models. The first clue comes from comparing the qualitative features of the arcs and the existing models. Despite differences in details, most of the previous models have a lensing potential with a strong tidal shear from the cluster ($\gamma \sim 0.1\text{--}0.4$). The galaxy dominates the potential for the close image (B), but the strong shear means that the cluster dominates the potential for the distant image (A). The distinction is important because in general a round host galaxy produces an image distorted tangentially relative to the mass that dominates the potential. As a result, for a circular host galaxy most previous models of Q 0957+561 would predict a B arc tangential to the galaxy (as observed), and an A arc tangential to the cluster – i.e. stretched *radially* relative to the lens galaxy, opposite what is observed. These lens models can produce an A image tangential to the galaxy only if the source galaxy is highly flattened and oriented at just the right angle. In other words, we must either invoke a very special source configuration or conclude that the standard Q 0957+561 models have generic problems.

We can quantify these problems by using the arc modeling technique described in §3.3 to predict the structure of the B arc for each model and compare it to the observed B arc. (Recall that this technique uses the observed A arc to construct the source, so models always reproduce the A arc correctly and hence are evaluated by examining the B arc.) Figures 2 and 3 show the observed and predicted models arcs for previous power law models, while Figure 4 shows the arcs for FGS models; Figure 5 shows the intrinsic source inferred for two of the models. Table 3 includes the quantitative $\bar{\chi}_{arc}^2$ estimates for the models.

All of these models are inconsistent with the structure of the B arc, both visually and in terms of $\bar{\chi}_{arc}^2$. Although the predicted arcs differ among the various models, there are two common features. First, in some of the models (notably those with a circular lens galaxy) the predicted B arc has a pair of bright ridges not seen in the observed B arc. Models that produce such ridges are strongly inconsistent with the data; they have $\bar{\chi}_{arc}^2$ statistics no better than 5.0 and as poor as 10.8. Second, the models generally fail to predict the correct shape for the B arc at low surface brightness levels. The predicted arcs have too much curvature and do not match the northeast extension of the observed arc. The failure to match even the rough shape (extent and curvature) of the B arc illustrates the point explained above: if the potential near the A image is dominated by the cluster shear, reproducing the A arc requires a flattened source (e.g. the Barkana/SPEMD model in Figure 5) that is distorted into a highly curved B arc. The existing models cannot match the arcs better than $\bar{\chi}_{arc}^2 = 2.2$, which given the large number of arc constraints means that these models are formally excluded at an extremely high significance level.

The models arcs also illustrate a crucial limitation of the broken power law models of Bernstein & Fischer (1999), represented here by the DM2+C2 model in Figure 3. These models use independent elliptical power law models in different radial zones to mimic the ellipticity and orientation

variations in the observed lens galaxy. The problem is that the density is discontinuous across the zone boundary, which leads to a discontinuity in the predicted B arc. The discontinuity does not affect the quantitative $\bar{\chi}_{arc}^2$ statistic because it occurs outside our mask, but it is qualitatively unacceptable. Combining this with the inability of the broken power law models to match normal rotation curves emphasizes that the models are physically unacceptable. The need for a more physically reasonable way to include ellipticity and orientation variations motivates our introduction of the double pseudo-Jaffe models.

Although the previous models do not correctly reproduce the distortions of the host galaxy, they do reveal a model-independent qualitative feature of the lensing. Part of the quasar host galaxy is doubly-imaged like the quasar, but a small region crosses the lensing caustic and is quadruply-imaged (see Figure 5). Arc A is a single distorted image of the host galaxy, but arc B is a combination of the three remaining images of the quadruply-imaged and the one remaining image of the doubly-imaged region. This fact explains why the A and B arcs have such different geometries. It also implies that with the current observations of the arcs, most of the constraints come from the small region of the host galaxy that is quadruply-imaged. A deeper image of the arcs should reveal a complete Einstein ring that would strengthen the constraints by using more of the host galaxy (see §6).

In summary, the host galaxy arcs in Q 0957+561 offer a strong new probe of the global shape of the lensing potential, and they show that existing lens models converged to the wrong potential. Generically, the previous models have too much shear from the cluster. The failure to fit the arcs is a common problem of models that combine strong constraints from the sub-milli-arcsecond structure of the quasar jets with oversimplified circular or elliptical lens models. It rules out existing models of the system, together with the bounds on H_0 drawn from them.

5. Successful new models

Two goals motivate our search for new models of Q 0957+561. First, if we want to use the VLBI constraints with sub-milli-arcsecond precision, we must be sensitive to details of the lens galaxy structure such as its radially varying ellipticity and orientation. We used double pseudo-Jaffe models (see §3.4) to incorporate such structure in a smooth and physically reasonable way. Second, we want to incorporate the powerful constraints from the host galaxy arcs into the modeling process, instead of using them for *a posteriori* tests as in §4. In this way we hope to break the environment degeneracy in a robust way. When we began to examine new models we found a range of solutions consistent with the data, so we adopted Monte Carlo techniques to sample this range. In this section we first describe the Monte Carlo techniques (§5.1), and then discuss the models and their implications for breaking the degeneracy between the galaxy and cluster (§5.2), the physical properties of the lens galaxy and cluster (§5.3), and the Hubble constant (§5.4).

5.1. Monte Carlo techniques

To explore our model space, we picked random values for the non-linear model parameters, using restricted but physically-motivated ranges:

- Galaxy ellipticity: There are no successful models with an outer ellipticity below 0.3. We believed models with an ellipticity larger than 0.7 to be implausible. Hence we considered $0.3 \leq e_2 \leq 0.7$ for the outer ellipticity. In models with an ellipticity gradient the inner ellipticity can be small, so we considered $0 \leq e_1 \leq 0.7$.
- Galaxy orientation: In the observed lens galaxy the PA varies from $\sim 40^\circ$ to $\sim 60^\circ$ (Bernstein et al. 1997). We expect the mass to be roughly aligned with the light (to within $\sim 10^\circ$; Keeton et al. 1998), so we considered $30^\circ \leq (\text{PA}_1, \text{PA}_2) \leq 70^\circ$ for the inner and outer position angles.
- Galaxy scale lengths: We fixed the inner pseudo-Jaffe component to be singular ($s_1 = 0$) and the outer component to have a cut-off radius $a_2 = 30''$ (see §3.6). For the cut-off radius of the inner component (a_1) and the core radius of the outer component (s_2) we considered $0''.1 \leq (a_1, s_2) \leq 4''$.
- Cluster direction angles: Galaxy counts and the weak lensing measurement suggest that the cluster has its mass concentration toward $\theta_{clus} \sim 55^\circ$ (Fischer et al. 1997). For reasonable cluster models the shear angle θ_γ points roughly to the cluster center (see §3.5), so we considered shear angles in the range $30^\circ \leq \theta_\gamma \leq 70^\circ$. We were less restrictive with the gradient angle θ_σ and required only that it be in the same quadrant as the cluster, $0^\circ \leq \theta_\sigma \leq 90^\circ$.

Given values for these parameters, we fixed the four remaining parameters (b_1, b_2, γ, σ) using the constraints from the quasar core and jet positions (see §3.6). Our limited parameter ranges may omit some models that are formally consistent with the data, but they span what we expect for physically reasonable models.

We tabulated models that fit the data at the 95% confidence level. With $N = (2, 4, 6)$ constraints this is equivalent to $\chi^2 \leq (5.99, 9.49, 12.59)$ (e.g. Press et al. 1992, §§6.2 and 15.6). We applied these thresholds to the constraints from the quasars and the optical Blobs and Knots both separately and jointly: we required $\chi^2_{flux} \leq 5.99$ for the flux ratios of the quasar cores and jets (2 constraints), $\chi^2_{bk} \leq 9.49$ for the positions of the optical Blobs and Knots (4 constraints), and $\chi^2_{flux} + \chi^2_{bk} \leq 12.59$ for the 6 joint constraints. We did not impose constraints from the less reliable Blob and Knot flux ratios. We considered different thresholds for the arc constraints, as discussed below. Note that it was not useful to combine all the constraints into a total χ^2/DOF because the number of constraints from the arcs is so large.

The Monte Carlo technique is not especially efficient; we examined $\sim 10^7$ models and found of order 1000 models consistent with the data. However, examining that many models is not prohibitively time consuming. Most of the models can be ruled out quickly because they fail the

flux and Blob/Knot χ^2 cuts. For the remaining models, we first computed a fast $\bar{\chi}_{arc}^2$ using a 4 times undersampled arc map; only for promising models did we compute $\bar{\chi}_{arc}^2$ using the full arc map. The benefit of this brute force approach is the ability to identify and sample the wide range of models consistent with the data, and thereby estimate the full range of possible H_0 values.

We first considered models in which the inner and outer components of the model galaxy were fixed to have the same ellipticity and orientation; we found (3, 275, 832, 1575) models with $\bar{\chi}_{arc}^2 < (1.2, 1.3, 1.4, 1.5)$, whose properties are summarized in Figure 6. Next we allowed the inner and outer galaxy components to have different shapes, mimicking ellipticity and orientation gradients. For simplicity, we refer to such models as having a “twist,” even though that term formally describes only an orientation gradient. We found (25, 134, 286, 477) twist models with $\bar{\chi}_{arc}^2 < (1.2, 1.3, 1.4, 1.5)$, whose properties are summarized in Figure 7. Table 4 gives parameters and Figure 8 shows the predicted arcs for sample models of both types. We note that the number of successful models with a twist is smaller than the number of successful models without a twist. Introducing the twist enlarges the parameter space without necessarily increasing the space of successful models by the same amount; hence sampling the same total number of models yields fewer acceptable models. In the following sections we discuss models with $\bar{\chi}_{arc}^2 < 1.5$, but our conclusions would not change substantially if we lowered this threshold.

5.2. Breaking the galaxy/cluster degeneracy

The host galaxy arcs finally break the degeneracy between the lens galaxy shape and the cluster shear in Q 0957+561. First, they constrain the lens galaxy shape. Among the previous models, the three with the best fits to the arcs have $62^\circ < PA < 67^\circ$ (Table 3). In the new models, the bounds on the (outer) orientation of the lens galaxy are $55^\circ < PA < 66^\circ$ in models without a twist (Figure 6d) and $52^\circ < PA_2 < 68^\circ$ in models with a twist (Figure 7f). These ranges are consistent with the observed galaxy’s orientation of about $56 \pm 8^\circ$ (Bernstein et al. 1997). In other words, the arcs not only constrain the model galaxy’s orientation, they require that its mass distribution be at least roughly aligned with the light distribution; such alignment is also seen in other lens systems (Keeton et al. 1998). Also, in the new models the bounds on the (outer) ellipticity of the galaxy are $0.38 < e < 0.61$ in models without a twist (Figure 6c) and $0.35 < e_2 < 0.63$ in models with a twist (Figure 7e). These ranges are slightly higher than the ellipticity seen in the outer parts of the galaxy (Bernstein et al. 1997), but there is no *a priori* reason to expect the ellipticities of the dark halo and the light to be similar. These constraints on the lens galaxy shape span models with a wide range of lens galaxy mass profiles (controlled by the scale radii a_1 and s_2 ; see Figures 6b and 7b), ellipticity profiles (with or without a twist), and cluster contributions. Thus we believe that they are robust, and that the ability of the host galaxy arcs to finally constrain the galaxy shape is the most important result of our new models.

Second, the arcs place limits on the lensing contribution of the cluster. The new models have moderate or even small cluster shears (typically $\gamma \lesssim 0.05$; Figures 6e and 7g), which contrasts

with the strong shears in previous models. A small shear is required by the fact that both arcs are tangential to the lens galaxy (see §4). Also, including the 3rd order cluster term is important, as expected from the proximity of the cluster to the lens (Kochanek 1991). Most models have a cluster gradient amplitude in the range $0.006 < \sigma < 0.016$ (Figures 6g and 7i), so at the position of image A the 3rd order term is comparable to or even larger than the 2nd order term (see eq. 12). Because the cluster amplitudes are small, the corresponding direction angles θ_γ and θ_σ are poorly constrained (Figures 6f, 6h, 7h, and 7j). Nevertheless, the fact that they usually differ implies that the cluster cannot be spherical (see §3.5).

Unfortunately, even the arcs cannot uniquely determine the model. First, the cluster angles can adjust to accommodate the narrow but finite range of lens galaxies given above. Second, in models with a twist the inner component can take on all values of ellipticity and orientation in the ranges we allowed (Figures 7c and 7d). This is because the inner component is usually compact, so like the point mass in FGS lens models it serves mainly to correct a central mass deficit and the model is largely insensitive to the distribution of that mass. Both of these degeneracies affect the potential enough to produce a disappointingly wide range of Hubble constant values (see §5.4).

These conclusions are drawn from models using a Taylor series for the cluster potential. We also examined models treating the cluster using an elongated isothermal model with an arbitrary position, axis ratio, and orientation.⁵ The above conclusions about the galaxy properties still pertain, with one modification: in models with a twist the distribution of outer orientation angles gains a tail down to $PA_2 \sim 40^\circ$. The above conclusions about the cluster contributions also hold, except that the new bounds on the shear amplitude are $0.03 < \gamma < 0.11$. Since an isothermal cluster has $\gamma \approx \kappa_{clus}$, it is hard to obtain a small shear without essentially eliminating the cluster.

5.3. Properties of the galaxy and cluster

We introduced the double pseudo-Jaffe models in order to smoothly include ellipticity and orientation variations in the lens galaxy, but we must ask whether the models are physically plausible. Figure 9 shows the estimated density and circular velocity profiles for the models in Table 4. These profiles are only estimates because they require the full 3-d mass distribution, while lens models give only the projected distribution. We assumed that the intrinsic distributions are oblate spheroids viewed edge-on, and we computed the density and circular velocity profiles in the equatorial plane, neglecting any twist. The high inferred circular velocities ($v_c \sim 600 \text{ km s}^{-1}$) are misleading, because our models omit any convergence from the cluster and $v_c \propto (1 - \kappa_{clus})^{1/2}$, and because converting to an observed velocity dispersion involves systematic uncertainties in the stellar dynamics (see Romanowsky & Kochanek 1999). The qualitative features, however, are plausible. The inner and outer galaxy components generally combine to produce a rotation curve that is ap-

⁵For technical reasons, the isothermal cluster models we used had only approximate elliptical symmetry.

proximately flat, although in several models it turns up at small radii because the inner component of the pseudo-Jaffe models is compact. This effect, which also appears in FGS models because of the point mass, occurs because lensing constrains only the total mass enclosed by the B image ($r_B = 1.^{\prime\prime}0$), and if that mass is compact then it produces a rising rotation curve. We conclude that the fitted double pseudo-Jaffe models are fairly reasonable.

As for the cluster, recall that the host galaxy arcs require the shear to be small. At the same time, two independent estimates of the cluster mass suggest that the convergence from the cluster is $\kappa_{clus} \sim 0.2$. First, stellar dynamical modeling of the lens galaxy constrains its mass such that explaining the image separation requires a cluster convergence of $\kappa_{clus} = 0.20 \pm 0.12$ (Romanowsky & Kochanek 1999). Second, Fischer et al. (1997) and Bernstein & Fischer (1999) used weak lensing to measure the total mass inside an aperture centered on the lens galaxy. Subtracting the mass of a model lens galaxy then gives a model-dependent estimate of the remaining cluster mass (see eq. 10). With this technique all of our models yield $0.20 \leq \kappa_{clus} \leq 0.23$.

These results are surprising because with popular cluster models it is difficult to produce a shear that is much smaller than the convergence (Keeton 2000). Specifically, with a singular isothermal ellipsoid, $\gamma = \kappa_{clus}$ for all cluster positions, orientations, and axis ratios. Introducing a core radius allows $\gamma \lesssim \kappa_{clus}$, but the shear is substantially smaller than the convergence only if the lens galaxy is near or within the cluster core. If the cluster halo has the “universal” or NFW density profile (Navarro et al. 1996), $\gamma \lesssim \kappa_{clus}/2$ only inside $\sim 0.5r_s$, where r_s is the NFW scale length. For the observed cluster at redshift $z_l = 0.36$ with a velocity dispersion of $\sim 700 \text{ km s}^{-1}$ (Angonin-Willaime et al. 1994), the NFW scale length would be $r_s \sim 100 h^{-1} \text{ kpc}$ or $\sim 30''$ (e.g. Navarro et al. 1996). Combining these results with the estimates of the cluster contribution ($\gamma \lesssim 0.1$ or even $\lesssim 0.05$, and $\kappa_{clus} \sim 0.2$) suggests two possible conclusions about the cluster. On the one hand, if the cluster is ellipsoidal it must have a core or scale radius large enough to encompass the galaxy. Having the lens galaxy be in the cluster core would not be too surprising since it is the brightest galaxy in the cluster. On the other hand, the assumption of an ellipsoidal model for the cluster may not be correct, perhaps because of substructure.

5.4. Implications for the Hubble constant

Finally, we want to combine the lens models and the observed time delay and use eq. (3) to determine the Hubble constant H_0 . As discussed in §3.1, the inferred value of H_0 depends weakly on the other cosmological parameters; we quote results assuming $\Omega_0 = 1$ and $\Lambda_0 = 0$ and note that they would increase by 5.8% (4.5%) for an $\Omega_0 = 0.3$ open (flat) cosmology. Also, the mass sheet degeneracy implies $H_0 \propto (1 - \kappa_{clus})$ (see eq. 6), and κ_{clus} cannot be constrained by lens models. Thus if we write $H_0 = 100 h \text{ km s}^{-1} \text{ Mpc}^{-1}$, lensing directly measures only the combination $h/(1 - \kappa_{clus})$, which is what we quote in Tables 3 and 4 and Figures 6 and 7. We need an independent estimate of κ_{clus} in order to constrain H_0 itself.

We saw in §5.2 that the host galaxy arcs help break the degeneracy between the lens galaxy shape and the cluster shear, but they do not eliminate it entirely. The remaining freedom in the models is small in terms of the properties of the lens galaxy but large in terms of the Hubble constant. Models without a twist yield $1.1 \lesssim h/(1 - \kappa_{clus}) \lesssim 1.4$, with a tail down to $h/(1 - \kappa_{clus}) \approx 0.95$ (Figure 6). Allowing a twist in the lens galaxy broadens the distribution down to $h/(1 - \kappa_{clus}) \approx 0.85$ (Figure 7). In other words, within the lens models there is a $\pm 25\%$ variation in inferred values for the Hubble constant; this is independent of uncertainties in κ_{clus} . Most of this variation is related to a strong correlation between the lens galaxy ellipticity and the Hubble constant (Figures 6c, 7c, and 7e): flatter galaxies have deeper central potential wells when normalized to produce the same images.

Although the model uncertainties limit our ability to use Q 0957+561 to constrain the Hubble constant, we might invert our thinking and ask what properties of the lens model are required to be consistent with local distance ladder determinations of H_0 (e.g. Mould et al. 1999). Assuming a cluster convergence $\kappa_{clus} \sim 0.2$ (see §5.3), obtaining $H_0 \lesssim 80 \text{ km s}^{-1} \text{ Mpc}^{-1}$ requires a lens galaxy that is relatively round in the center ($e_1 \lesssim 0.30$) and moderately flattened in the outer parts ($0.35 \lesssim e_2 \lesssim 0.56$). These bounds bolster the suggestion that the lens galaxy must have a mass distribution with an ellipticity gradient fairly similar to that seen in the light distribution.

6. Conclusions

We have detected large, distorted images of the quasar host galaxy in the gravitational lens Q 0957+561. In the H band (rest frame R), the host galaxy appears as two long ($\sim 5''$) arcs stretched tangentially relative to the lens galaxy. Previously published models of Q 0957+561 fail to predict the correct shape for the host galaxy arcs. This failure rules out those models and any conclusions about the value of the Hubble constant drawn from them.

The problem with the previous models is that they oversimplified the mass distribution for the lens galaxy, so they had to adjust the large-scale features of the model (the galaxy shape and the cluster shear) in order to fit small-scale constraints (the VLBI jets, with ~ 0.1 milli-arcsecond errorbars). Without strong constraints on the global shape of the lensing potential, each class of models happily converged to a best-fit solution with the wrong global structure. The failure of these models presents two important lessons (also see Kochanek 1991; Bernstein et al. 1993; Mao & Schneider 1998; Bernstein & Fischer 1999). First, when the constraints are extremely precise it is necessary to include the full complexity of the structure of the lens galaxy. Second, it is important to carefully explore the full range of possible models before leaping to conclusions about the value of the Hubble constant and its uncertainties.

Two improvements are crucial to finding better models. First, the host galaxy arcs finally provide enough constraints to separately determine both the lens galaxy shape and the cluster shear, and they must be incorporated into the modeling process. Second, models for the lens galaxy

must allow internal structure similar to that seen in the observed galaxy, which for Q 0957+561 means a radially varying ellipticity and orientation. Although the mass need not exactly trace the light, it must be given the same freedoms lest we oversimplify the models. We introduced a new class of lens models, the double pseudo-Jaffe models, that smoothly incorporate an ellipticity gradient and isophote twist.

Our models lead to several new conclusions about the system. First, the shape of the lens galaxy’s mass distribution must be surprisingly similar to the shape of its luminosity distribution. The mass distribution must be moderately flattened and roughly aligned with the light distribution. Such alignment between the mass and the light is also seen in other gravitational lenses (Keeton et al. 1998), but was not seen in previous models of Q 0957+561. Second, the shear from the cluster must be small ($\gamma \lesssim 0.1$), in marked contrast with the moderate or strong shears seen in previous models ($\gamma \sim 0.1\text{--}0.4$). The small shear combined with an estimated convergence $\kappa_{clus} \sim 0.2$ implies that the cluster potential must be approximately centered on the lens galaxy. Unfortunately, the current observations of the host galaxy cannot fully determine the lens model. There are still freedoms related to several direction angles that describe the cluster and to the amplitudes of the ellipticity and orientation gradients, and they leave a 25% uncertainty in the inferred value of the Hubble constant.

However, there are two promising prospects for further improving the constraints on this systems. First, the substantial progress we have found is based on a 2800-second H band image. A deeper image with a refurbished NICMOS camera should show a complete Einstein ring image. Since an Einstein ring probes the potential all the way around the lens galaxy, it is extremely useful for determining both the lens model and the intrinsic shape of the host galaxy (see Keeton, Kochanek & McLeod 2000). Filling in the gaps in the Q 0957+561 ring should eliminate the remaining uncertainties in the models. Second, X-rays from the cluster gas have been detected (Chartas et al. 1998), but the image resolution was poor and the signal was dominated by X-rays from the quasar images. New high-resolution X-ray observations to map the cluster gas would constrain the cluster potential and help determine the cluster angles that are still unknown (namely the angle to the cluster center and the angle of the cluster’s density gradient at the lens). Combining deeper infrared and X-ray imaging would thus dramatically improve the constraints on the models and allow consistency checks of the cluster potential. Improved X-ray imaging would also further improve the mass estimates of the cluster for breaking the mass sheet degeneracy.

Distorted images of the host galaxy have now been observed in four of the time delay lenses (Q 0957+561, PG 1115+080, B 1600+434, and B 1608+656; see Impey et al. 1998; Kochanek et al. 1999). As we have illustrated, images of the host galaxy are a powerful constraint on models of the system and hence on the uncertainties in the value of H_0 derived from the time delay measurements. To date, host galaxies have been thought of mainly as pleasant bonuses in relatively shallow images targeting the lens galaxies. Taking full advantage of the host galaxies will require deeper images focused on the host galaxies themselves. Such images hold great promise for breaking common degeneracies in lens models and allowing gravitational lensing to map in detail the mass distributions

of distant galaxies, to probe the potentials of lens galaxy environments, and to determine a robust and independent measurement of the Hubble constant at cosmological distances.

Acknowledgements: We thank Gary Bernstein for discussions and comparisons with new optical data. Support for the CASTLES project was provided by NASA through grant numbers GO-7495 and GO-7887 from the Space Telescope Science Institute, which is operated by the Association of Universities for Research in Astronomy, Inc., under NASA contract NAS 5-26555.

A. Appendix: Comparing lens models

Table 3 summarizes results from models of Q 0957+561 by Grogin & Narayan (1996), Barkana et al. (1999), Bernstein & Fischer (1999), and Chae (1999). The various authors reported results in different ways. Sorting out the differences can be confusing, so we converted all the results to a standard form and explain the conversions here.

First, Bernstein & Fischer (1999) and Chae (1999) quoted an ellipticity parameter ϵ that is related to the axis ratio q by $q^2 = (1-\epsilon)/(1+\epsilon)$. We report the true ellipticity $e = 1-q$. (Bernstein & Fischer called their ellipticity parameter e , but it played the same role as ϵ here.)

Second, different authors quoted results for the Hubble constant in different ways. In general, lens models can determine only the combination $h/(1 - \kappa_{clus})$ where $h = H_0/(100 \text{ km s}^{-1} \text{ Mpc}^{-1})$ and $\kappa_{clus} = \Sigma_{clus}/\Sigma_{crit}$ is the surface mass density of the cluster (in critical units) at the position of the lens. Models that use a multipole expansion for the cluster (an external shear or 3rd order cluster, see eq. 12) offer no constraints on κ_{clus} . Models that use an actual mass distribution for the cluster do predict κ_{clus} : an isothermal sphere that has core radius s and is located a distance d from the lens produces $\kappa_{clus} = b/(2\xi)$ and shear $\gamma_{clus} = (bd^2)/[2\xi(s+\xi)^2]$, where $\xi = \sqrt{s^2 + d^2}$ and b is a mass parameter such that $M(R) = \pi\Sigma_{crit}b(\sqrt{s^2 + R^2} - s)$. However, the κ_{clus} prediction is not unique because varying the cluster's shape and profile can change κ_{clus} (and γ_{clus}) without changing the goodness of fit (see Chae 1999 for examples). Hence we describe these cluster models in terms of an equivalent external shear with magnitude $\gamma_{eff} = \gamma_{clus}/(1 - \kappa_{clus})$ (see Grogin & Narayan 1996; Barkana et al. 1999). In Table 3 we quote the magnitude of the external shear (γ , or γ_{eff} in the isothermal sphere cluster models) and the Hubble constant combination $h/(1 - \kappa_{clus})$. We note that if the cluster is a singular isothermal sphere, $(1 - \kappa_{clus}) = (1 + \gamma_{eff})^{-1}$ (see Barkana et al. 1999). The estimates of $h/(1 - \kappa_{clus})$ can be translated into actual estimates for H_0 using the weak lensing measurement of the cluster mass (see §3.2).

Third, different authors used slightly different definitions of χ^2 . We did *not* convert χ^2 values; we used what the authors reported.

Finally, we corrected several apparent typographical errors. Barkana et al. (1999) claimed that their galaxy orientation angle θ was a position angle, but in fact the position angle was $90^\circ - \theta$

and this is what we quote. Bernstein & Fischer (1999) quoted angles measured from the positive x -axis. Their formalism is self-consistent, except that their eq. (16) needs a minus sign in front of the γ term. We report the Bernstein & Fischer (1999) angles as position angles. Finally, for the Bernstein & Fischer (1999) 3rd order cluster models there appears to be a difference of a factor of 2 between the amplitude of 3rd order cluster term as written in their eq. (16) and as reported in their Table 3. We quote values consistent with their eq. (16).

B. Appendix: The pseudo-Jaffe ellipsoid

A standard Jaffe (1983) model has a 3-dimensional density distribution $\rho \propto m^{-2} (m + a)^{-2}$ where m is an ellipsoidal coordinate and a is the break radius. For lensing it is more convenient to use a modified density distribution $\rho \propto (m^2 + s^2)^{-1} (m^2 + a^2)^{-1}$ where a is again the break radius, and we have added a core radius $s < a$. For this model the projected surface mass density, in units of the critical surface density for lensing, is

$$\frac{\Sigma}{\Sigma_{crit}} = \frac{b}{2} \left[(m^2 + s^2)^{-1/2} - (m^2 + a^2)^{-1/2} \right], \quad (B1)$$

where the mass normalization parameter b is chosen to match the lensing critical radius in the limit of a singular isothermal sphere ($s \rightarrow 0$, $a \rightarrow \infty$, $q \rightarrow 1$). Eq. (B1) defines what we call the pseudo-Jaffe ellipsoid. Its projected surface density is roughly constant for $R \lesssim s$, falls as R^{-1} for $s \lesssim R \lesssim a$, and falls as R^{-3} for $R \gtrsim a$; its total mass is $M = \pi \Sigma_{crit} q b (a - s)$. The ellipsoid coordinate m can be written in terms of the projected axis ratio q and the position angle PA (measured East of North) as

$$m^2 = \frac{R^2}{2q^2} \left[(1 + q^2) + (1 - q^2) \cos 2(\theta - \text{PA}) \right]. \quad (B2)$$

The pseudo-Jaffe lens model is easy to compute because it is written as the difference of two softened isothermal ellipsoids, whose analytic lensing properties are known (Kassiola & Kovner 1993; Kormann, Schneider & Bartelmann 1994; Keeton & Kochanek 1998). This model has been used previously by de Zeeuw & Pfenniger (1988), Brainerd, Blandford & Smail (1996), and Keeton & Kochanek (1998).

In the limit of a singular model ($s = 0$), the pseudo-Jaffe model is an example of a general class of “cuspy” lens models with $\rho \propto m^{-\gamma} (m^2 + a^2)^{(\gamma-4)/2}$. These models are a more realistic family for real galaxies than the softened power law models, and are discussed by Muñoz, Kochanek & Keeton (2000).

The pseudo-Jaffe model is related to the King model used in FGS lens models. The standard approach is to approximate the King model with a combination of isothermal models (Young et al. 1980),

$$\frac{\Sigma}{\Sigma_{crit}} = \frac{2.12b}{\sqrt{m^2 + 0.75r_s^2}} - \frac{1.75b}{\sqrt{m^2 + 2.99r_s^2}}. \quad (B3)$$

The King model has a single scale radius r_s , while the pseudo-Jaffe model has independent core and break radii. Also, in the King model the coefficients of the two terms differ, while in the pseudo-Jaffe model they are the same.

REFERENCES

Angonin-Willaime, M. C., Soucail, G., & Vanderriest, C. 1994, A&A, 291, 411

Barkana, R. 1996, ApJ, 468, 17

Barkana, R. 1997, ApJ, 489, 21

Barkana, R., Lehár, J., Falco, E. E., Grogin, N. A., Keeton, C. R., & Shapiro, I. I. 1999, ApJ, 523, 54

Bernstein, G., Fischer, P., Tyson, J. A., & Rhee, G. 1997, ApJ, 483, L79

Bernstein, G., & Fischer, P. 1999, AJ, 118, 14

Bernstein, G. M., Tyson, J. A., & Kochanek, C. S. 1993, AJ, 105, 816

Biggs, A. D., Browne, I. W. A., Helbig, P., Koopmans, L. V. E., Wilkinson, P. N., Perley, R. A. 1999, MNRAS, 304, 349

Brainerd, T. G., Blandford, R. D., & Smail, I. 1996, ApJ, 466, 623

Chae, K.-H. 1999, ApJ, 524, 582

Chartas, G., Chuss, D., Forman, W., Jones, C., & Shapiro, I. 1998, ApJ, 504, 661

Courbin, F., Magain, P., Keeton, C. R., Kochanek, C. S., Vanderriest, C., Jaunsen, A. O., & Hjorth, J. 1997, A&A, 324, L1

Falco, E. E., Gorenstein, M. V., & Shapiro, I. I. 1985, ApJ, 289, L1

Falco, E. E., Gorenstein, M. V., & Shapiro, I. I. 1991, ApJ, 372, 364

Falco, E. E., Shapiro, I. I., Moustakas, L. A., & Davis, M. 1997, ApJ, 484, 70

Falco, E. E., Kochanek, C. S., Lehár, J., McLeod, B. A., Impey, C. D., Keeton, C. R., Peng, C. Y., & Rix, H.-W. 1999, to appear in Gravitational Lensing: Recent Progress and Future Goals, ASP conference series, eds. T. Brainerd & C. S. Kochanek (also preprint astro-ph/9910025)

Fassnacht, C. D., Pearson, T. J., Readhead, A. C. S., Brownse, I. W. A., Koopmans, L. V. E., Myers, S. T., & Wilkinson, P. N. 1999, ApJ, 527, 498

Fischer, P., Bernstein, G., Rhee, G., & Tyson, J. A. 1997, A&A, 113, 521

Garrett, M. A., Calder, R. J., Porcas, R. W., King, L. J., Walsh, D., & Wilkinson, P. N. 1994, MNRAS, 270, 457

Garrett, M. A., Walsh, D., & Carswell, R. F. 1992, MNRAS, 254, 27p

Grogin, N. A., & Narayan, R. 1996, ApJ, 464, 92; erratum, ApJ, 473, 570

Haarsma, D. B., Hewitt, J. N., Lehár, J., & Burke, B. F. 1999, ApJ, 510, 64

Hjorth, J., Burud, I., Jaunsen, A. O., & Østensen, R. 1999, to appear in Gravitational Lensing: Recent Progress and Future Goals, ASP conference series, eds. T. Brainerd & C. S. Kochanek

Impey, C. D., Falco, E. E., Kochanek, C. S., Lehár, J., McLeod, B. A., Rix, H.-W., Peng, C. Y., & Keeton, C. R. 1998, ApJ, 509, 551

Jackson, N., Nair, S., & Browne, I. W. A. 1997, in Observational cosmology with the new radio surveys, eds. M. Bremer, N. Jackson & I. Perez-Fournon (Dordrecht: Kluwer)

Kassiola, A., & Kovner, I. 1993, ApJ, 417, 450

Keeton, C. R., & Kochanek, C. S. 1997, ApJ, 487, 42

Keeton, C. R., & Kochanek, C. S. 1998, ApJ, 495, 157

Keeton, C. R., Kochanek, C. S., & Seljak, U. 1997, ApJ, 482, 604

Keeton, C. R., Kochanek, C. S., & Falco, E. E. 1998, ApJ, 509, 561

Keeton, C. R., Kochanek, C. S., & McLeod, B. A. 2000, in preparation

Keeton, C. R. 2000, in preparation

Kochanek, C. S. 1991, ApJ, 382, 58

Kochanek, C. S., & Narayan, R. 1992, ApJ, 401, 461

Kochanek, C. S., Falco, E. E., Impey, C. D., Lehár, J., McLeod, B. A., & Rix, H.-W. 1999, in After the Dark Ages: When Galaxies Were Young (9th Annual October Astrophysics Conference in Maryland), eds. S. Holt & E. Smith (also preprint astro-ph/9811111)

Koopmans, L. V. E., & Fassnacht, C. D. 1999, ApJ, 527, 513

Koopmans, L. V. E., et al. 1999, MNRAS, 303, 727

Kormann, R., Schneider, P., & Bartelmann, M. 1994, A&A, 284, 285

Kundić, T., Turner, E. L., Colley, W. N., Gott, J. R., Rhoads, J. E., Wang, Y., Bergeron, L. E., Gloria, K. A., Long, D. C., Malhorta, S., & Wambsganss, J. 1997, ApJ, 482, 75

Lehár, J., Falco, E. E., Kochanek, C. S., McLeod, B. A., Muñoz, J. A., Impey, C. D., Rix, H.-W., Keeton, C. R., & Peng, C. Y. 1999, ApJ, submitted (preprint astro-ph/9909072)

Lovell, J. E. J., Jauncey, D. L., Reynolds, J. E., Wieringa, M. H., King, E. A., Tzioumis, A. K., McCulloch, P. M., & Edwards, P. G. 1998, ApJ, 508, L51

Mao, S., & Schneider, P. 1998, MNRAS, 295, 587

Mould, J. R., et al. 1999, ApJ, submitted (preprint astro-ph/9909260)

Muñoz, J. A., Kochanek, C. S., & Keeton, C. R. 2000, in preparation

Navarro, J., Frenk, C. S., & White, S. D. M. 1996, ApJ, 462, 563

Press, W. H., Teukolsky, S. A., Vetterling, W. T., & Flannery, B. P. 1992, Numerical Recipes in C: The Art of Scientific Computing, Second Edition (New York: Cambridge Univ. Press)

Refsdal, S. 1964, MNRAS, 128, 307

Refsdal, S. 1966, MNRAS, 132, 101

Rhee, G. 1991, Nature, 350, 211

Romanowsky, A. J., & Kochanek, C. S. 1999, ApJ, 516, 18

Saha, P., & Williams, L. L. R. 1997, MNRAS, 292, 148

Schechter, P. L., et al. 1997, ApJ, 475, L85

Schild, R., & Thomson, D. J. 1995, AJ, 109, 1970

Schneider, P., Ehlers, J., & Falco, E. E. 1992, Gravitational Lenses (New York: Springer)

Seljak, U. 1994, ApJ, 436, 509

Tonry, J. L., Franx, M., 1999, ApJ, 515, 512

Walsh, D., Carswell, R. F., & Weymann, R. J. 1979, Nature, 279, 381

Young, P., Gunn, J. E., Kristian, J., Oke, J. B., & Westphal, J. A. 1980, ApJ, 241, 507

Young, P., Gunn, J. E., Oke, J. B., Westphal, J. A., & Kristian, J. 1981, ApJ, 244, 736

de Zeeuw, T., & Pfenniger, D. 1988, MNRAS, 235, 949

TABLE 1
SUMMARY OF OBSERVATIONS

UT Date	Camera/Filter	Duration	N/Dith	Detect (mag/ \square'')	Source
1998.05.30	NIC2/F160W	700 s	4/3''.0	20.7	GO-7887, Falco
1995.11.19	WFPC2/F814W	160-900 s	2/0''.2	22.6	GO-5979, Rhee
1995.11.19	WFPC2/F555W	2300 s	14/2''.2	25.2	GO-5979, Rhee

NOTE.— “Duration” refers to individual exposures. “N/Dith” indicates the number of exposures and largest dither separation. The detection limit corresponds to 3σ above the sky.

TABLE 2
ASTROMETRY AND PHOTOMETRY

ID	z	RA ($''$)	Dec ($''$)	H (mag)	V-I (mag)	V-H (mag)	I-H (mag)	R_e ($''$)	$1 - b/a$	PA ($^\circ$)
A	1.41	$\equiv 0$	$\equiv 0$	15.60 ± 0.03	0.38 ± 0.13	1.49 ± 0.09	1.11 ± 0.10			
B	1.41	1.229 ± 0.005	-6.048 ± 0.004	15.68 ± 0.03	0.34 ± 0.11	1.43 ± 0.07	1.09 ± 0.09			
G1	0.36	1.406 ± 0.006	-5.027 ± 0.005	15.14 ± 0.09	1.95 ± 0.07	3.92 ± 0.07	1.97 ± 0.04	2.23 ± 0.20	0.20 ± 0.01	44 ± 3
G2		8.816 ± 0.016	-2.942 ± 0.005	17.92 ± 0.04	1.90 ± 0.35	3.96 ± 0.25	2.06 ± 0.24	0.43 ± 0.02	0.45 ± 0.03	62 ± 2
G3		5.04 ± 0.01	0.63 ± 0.02	21.5 ± 0.2	1.8 ± 0.2	3.3 ± 0.2	1.5 ± 0.2	0.10 ± 0.03	0.17 ± 0.04	86 ± 36
G4		-0.551 ± 0.009	-5.498 ± 0.009	22.2 ± 0.1	1.6 ± 0.3	3.8 ± 0.3	1.7 ± 0.1	$\equiv 0$		

NOTE.— The photometric structure (R_e , $1 - b/a$, PA) of the lens galaxy G1 comes from a simple de Vaucouleurs model, neglecting the radially varying ellipticity and major axis found by Bernstein et al. (1997). The magnitude uncertainties (column 5) include the uncertainties in the photometric structure of the galaxy, while the color uncertainties (columns 6–8) are determined for a fixed photometric structure. Object G4 was unresolved, so we fit it with a point source. G3 and G4 correspond to faint objects labeled Blobs 7 and 1 (respectively) in the deep optical images of Bernstein et al. (1997).

TABLE 3
HISTORICAL MODELS OF Q 0957+561

Model ⁽¹⁾	Cluster ⁽²⁾		Ellipticity		Radial Structure			$\chi^2/\text{DOF}^{(5)}$	$\bar{\chi}_{\text{arc}}^2{}^{(6)}$	$h/(1 - \kappa_{\text{clus}})^{(7)}$
	γ	θ_γ (°)	Misc.	ϵ	PA (°)	$\alpha^{(3)}$	$M_{\text{pm}}^{(4)}$			
Grogin/SPLS	0.298	67.4				1.08	Core radius 0'058	41.4/6	5.71	0.82
Barkana/SPLS	0.258	66.4				1.16	Singular	253/11	4.99	0.78
Bernstein/SPLS+C2	0.214	64.0				1.16	Singular	87.9/7	2.91	—
Barkana/SPEMD	0.364	51.9		0.531	-56.2	1.01	Core radius 0'17	89.1/9	6.08	0.73
Chae/SPEMD+CL	0.128	51.8	$d = 9''$, $s = 4''$	0.170	64.0	1.28	Singular	49.6/25	2.24	0.74
Bernstein/DM1+C2	0.377	60.0		0.500	-33.4	1.19	Singular	36.4/6	5.35	—
Bernstein/DM1+C3S	0.135	49.0	$\sigma = 0.0078$, $\theta_\sigma = 79^\circ$	0.358	77.7	1.17	Singular	6.1/4	3.57	0.92
Bernstein/DM2+C2 ⁽⁸⁾	0.142	57.0		0.333	-80.3	1.26	Singular, break	7.2/2	3.91	—
				0.170	89.7	1.34	radius 1'06			
Grogin/FGS	0.377	67.8				2.54	Scale radius 0'63	19.0/5	7.04	0.94
Barkana/FGS	0.209	65.0				10.7	Scale radius 2'58	270/10	10.83	0.79
Barkana/FGSE	0.083	63.4		0.555	67.3	9.25	Scale radius 1'59	48.0/8	2.70	1.33
Barkana/FGSE+CL	0.122	63.3	$d = 15'34$, $s = 0$	0.495	61.9	6.99	Scale radius 1'39	41.3/7	2.24	1.27

NOTE.—We converted results quoted by the various authors into a standard form, and we corrected several apparent typographical errors in the original papers. See Appendix A for details.

(1) The various types of models are described in §§3.4 and 3.5. Galaxy models: SPLS = power law sphere; SPEMD = DM1 = power law ellipsoid; DM2 = broken power law model with one power law ellipsoid inside the break radius and an independent power law ellipsoid outside the break radius (the density is discontinuous across the break). Cluster models: no specification = C2 = external shear; C3S = 3rd order Taylor series; CL = isothermal sphere. The references are Grogin & Narayan (1996), Barkana et al. (1999), Bernstein & Fischer (1999), and Chae (1999).

(2) γ and θ_γ refer to the magnitude and position angle (North through East) of the external shear. For a 3rd order cluster (C3S), σ and θ_σ give the magnitude and position angle of the 3rd order terms in the potential (see §3.5). For an isothermal sphere (CL), s is the core radius, d and θ_γ are the distance and direction of the cluster from the lens galaxy, and γ is the amplitude of an equivalent external shear (see Appendix A).

(3) Power law exponent in the sense $\Sigma(R) \sim R^{\alpha-2}$ or $M(R) \sim R^\alpha$.

(4) Mass of central point mass in FGS models, in units of $10^{10} h^{-1} M_\odot$.

(5) Different studies used different definitions of χ^2 , and we quote the results directly without trying to convert them to a standard form.

(6) Our calculation of the χ^2 contribution from the arc constraints, as defined in §3.3.

(7) Implications for H_0 . In general the lens models determine only $h/(1 - \kappa_{\text{clus}})$ where $h = H_0/(100 \text{ km s}^{-1} \text{ Mpc}^{-1})$ and $\kappa_{\text{clus}} = \Sigma_{\text{clus}}/\Sigma_{\text{crit}}$ is the surface mass density of the cluster (in critical units) at the position of the lens. If the cluster is a singular isothermal sphere, $(1 - \kappa_{\text{clus}}) = (1 + \gamma)^{-1}$ (see the Appendix). These can be converted into H_0 estimates using the weak lensing mass estimate (see §3.2). Bernstein & Fischer (1999) gave H_0 results for the DM1+C3S model, but not for the other models quoted here.

(8) The two sets of parameters refer to the inner and outer power law ellipsoids.

TABLE 4
SAMPLE DOUBLE PSEUDO-JAFFE LENS MODELS

Component	Normalization	Core Radius	Cut-off Radius	Ellipticity	Orientation	Cluster	Cluster	χ^2	$h/(1 - \kappa)$	Comment
	b ('')	s ('')	a ('')	e	PA (°)	Amplitude	Angle (°)			
inner	12.06	[0]	0.117	0.470	58.37	$\gamma = 0.004$	$\theta_\gamma = 63.47$	flux: 1.76	1.041	Case 1a: no twist, best $\bar{\chi}^2_{arc}$
outer	5.52	1.124	[30]	0.470	58.37	$\sigma = 0.013$	$\theta_\sigma = 46.07$	blobs: 2.42		
inner	13.83	[0]	0.101	0.418	61.26	$\gamma = 0.004$	$\theta_\gamma = 51.28$	flux: 0.69	0.944	Case 1b: no twist, lowest H_0
outer	5.77	1.490	[30]	0.418	61.26	$\sigma = 0.014$	$\theta_\sigma = 39.04$	blobs: 6.17		
inner	3.89	[0]	3.596	0.614	58.30	$\gamma = 0.005$	$\theta_\gamma = 69.01$	flux: 5.82	1.361	Case 1c: no twist, highest H_0
outer	5.24	1.783	[30]	0.614	58.30	$\sigma = 0.011$	$\theta_\sigma = 73.74$	blobs: 6.55		
inner	2.51	[0]	0.532	0.053	64.59	$\gamma = 0.011$	$\theta_\gamma = 50.52$	flux: 3.66	0.971	Case 2a: twist, best $\bar{\chi}^2_{arc}$
outer	5.62	1.570	[30]	0.439	61.06	$\sigma = 0.015$	$\theta_\sigma = 39.14$	blobs: 6.51		
inner	1.84	[0]	1.651	0.004	49.02	$\gamma = 0.013$	$\theta_\gamma = 45.25$	flux: 5.05	0.852	Case 2b: twist, lowest H_0
outer	7.27	3.363	[30]	0.449	61.30	$\sigma = 0.014$	$\theta_\sigma = 39.39$	blobs: 6.45		
inner	4.67	[0]	3.763	0.691	56.12	$\gamma = 0.022$	$\theta_\gamma = 40.49$	flux: 5.33	1.379	Case 2c: twist, highest H_0
outer	5.26	1.931	[30]	0.573	61.75	$\sigma = 0.015$	$\theta_\sigma = 80.99$	blobs: 7.07		
								arc: 1.32		

NOTE.—Parameters for sample models with radial ellipticity and orientation variations (“twist”) or without (“no twist”). In all models, [· · ·] denotes a scale length held fixed (see §3.5).

Fig. 1.— (a) The raw F160W (H band) image of the Q 0957+561 system, using a logarithmic grayscale. The lens galaxy (G1) and quasar images (A and B) are labeled. The tickmarks on the frame are spaced by $1''$. (b) The residual image after subtracting the two quasars and the lens galaxy, plotted with a linear grayscale. The holes in the bright regions of the arcs are due to imperfect subtraction of the quasar images. (c) The residual image convolved with a $\sim 0''.076$ (1 pixel) FWHM Gaussian to enhance the visibility of low surface brightness features. The dotted contours are drawn at 2σ above the sky. The rectangular mask around the A arc shows the region used to construct the unlensed source, while the polygonal mask around the B arc shows the region used to compute χ^2_{arc} (see §3.3).

Fig. 2.— The observed (grayscale) and predicted (contours) arc structures for power law galaxy models. The grayscale is linear, and the solid contours are drawn at $2, 6, 10, \dots \times \sigma$ above the sky. The dotted contours are drawn for the observed image at 2σ . The tickmarks on the frames are again spaced by $1''$. We show the Grogan & Narayan (1996) SPLS model (top left), the Barkana et al. (1999) SPLS (top right) and SPEMD (bottom right) models, and the Chae (1999) SPEMD+CL model (bottom left). The galaxy is circular in the SPLS model and elliptical in the SPEMD models. The cluster is treated as an external shear in all models except for Chae/SPEMD+CL, in which it is treated as a softened isothermal sphere.

Fig. 3.— Power law galaxy models from Bernstein & Fischer (1999). The models are: SPLS+C2 (top left), DM1+C2 (top right), DM1+C3S (bottom left), and DM2+C2 (bottom right). For the galaxy, SPLS indicates a circular power law, DM1 indicates an elliptical power law, and DM2 indicates an elliptical broken power law. For the cluster, C2 refers to a 2nd order multipole expansion for the cluster (an external shear), and C3S refers to a 3rd order expansion.

Fig. 4.— FGS-type models. We show the Grogan & Narayan (1996) FGS model (top left), as well as the Barkana et al. (1999) FGS (top right), FGSE (bottom left), and FGSE+CL (bottom right) models. FGS refers to a circular galaxy and FGSE refers to an elliptical galaxy; both represent the cluster as an external shear. The FGSE+CL model represents the cluster as a singular isothermal sphere.

Fig. 5.— The intrinsic source structure inferred for two sample lens models. The grayscale and contours are the same as in Figures 2–4, and again the tickmarks on the frames are spaced by $1''$. The heavy curves show the lensing caustics. The cuspy diamond-shaped curve is the tangential caustic, and the round curve in the Barkana/SPEMD model is the radial caustic. In the Barkana/FGSE+CL model, the radial caustic is formally at infinity because of the point mass. A source inside the tangential caustic produces 4 images, between the tangential and radial caustics produces 2 images, and outside the radial caustic produces 1 image. The source for the Barkana/FGSE+CL model is offset because of the deflection produced by the isothermal cluster model.

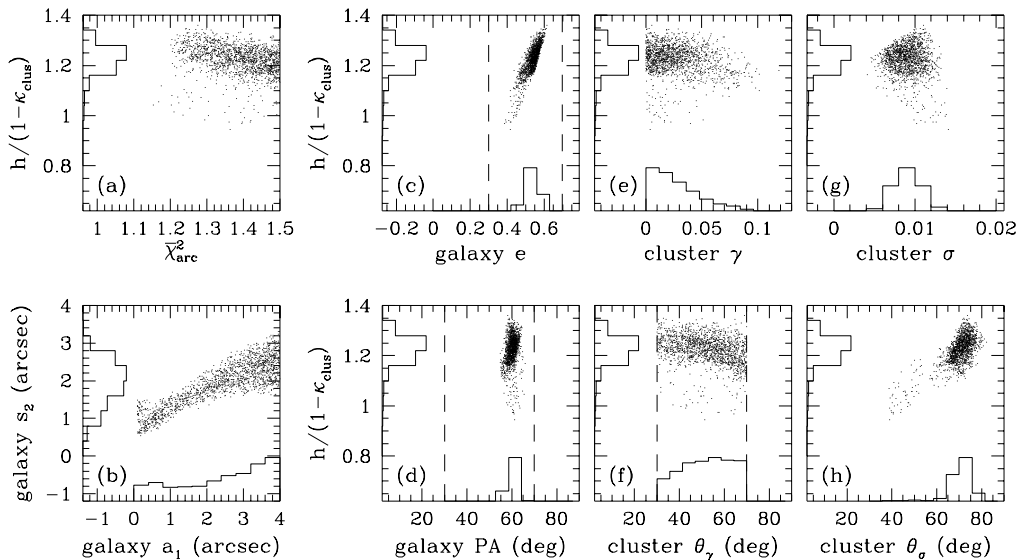


Fig. 6.— Results for models without radial ellipticity and orientation variations. The points indicate the values for the parameters, $\bar{\chi}_{arc}^2$, and Hubble constant for individual models, while the histograms show the corresponding distributions (normalized to have the same peak value). We quote Hubble constant results in terms of the quantity $h/(1 - \kappa_{clus})$ that is constrained by the lens models; the Hubble constant histograms are the same in all panels. The vertical dashed lines indicate the parameter ranges we examined, except the range for θ_σ is outside the figure ($0^\circ \leq \theta_\sigma \leq 90^\circ$). There were no explicit bounds placed on the cluster amplitudes γ and σ .

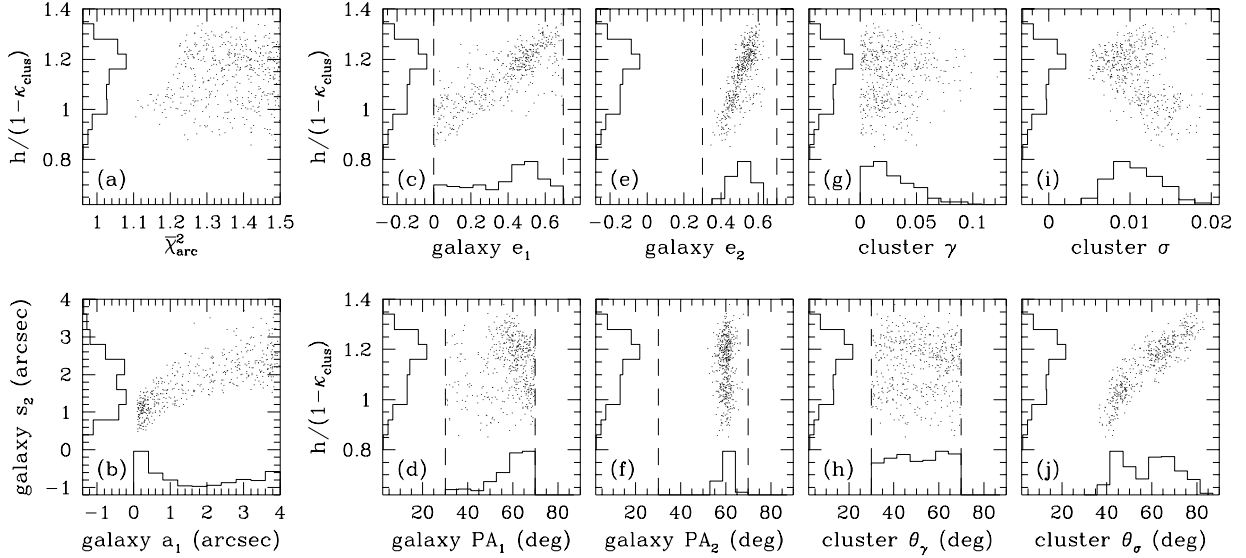


Fig. 7.— Similar to Figure 6 but for models with radial ellipticity and orientation variations.

Fig. 8.— The observed and predicted arc structures for four of the new models given in Table 4. Cases 1a and 1b refer to the no-twist models that have the best fit to the host galaxy arcs and the lowest value of H_0 , respectively. Cases 2a and 2b refer to the twist models with the same properties.

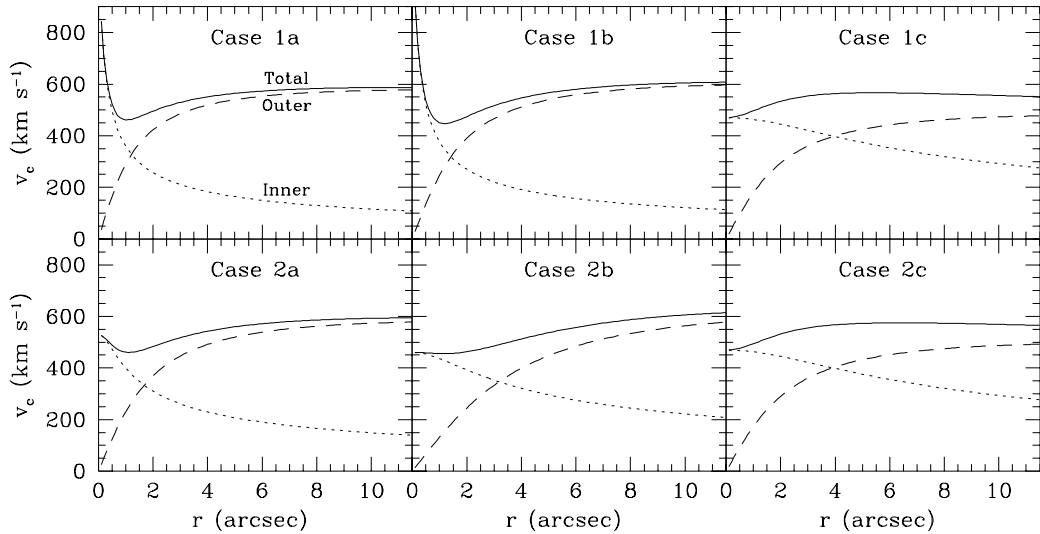


Fig. 9.— Estimates of the equatorial circular velocity profile for the models given in Table 4, assuming that the 3-d mass distributions are oblate spheroids viewed edge-on. The dotted and dashed curves show the contributions from the inner and outer pseudo-Jaffe components, respectively, and the solid curves show the total rotation curves. For reference, the quasar images A and B are $5.^{\circ}2$ and $1.^{\circ}0$ from the center of the lens galaxy. Note that the high inferred circular velocities ($v_c \sim 600 \text{ km s}^{-1}$) are misleading, as explained in the text.

This figure "fig1.gif" is available in "gif" format from:

<http://arxiv.org/ps/astro-ph/0001500v1>

This figure "fig2.gif" is available in "gif" format from:

<http://arxiv.org/ps/astro-ph/0001500v1>

This figure "fig3.gif" is available in "gif" format from:

<http://arxiv.org/ps/astro-ph/0001500v1>

This figure "fig4.gif" is available in "gif" format from:

<http://arxiv.org/ps/astro-ph/0001500v1>

This figure "fig5.gif" is available in "gif" format from:

<http://arxiv.org/ps/astro-ph/0001500v1>

This figure "fig8.gif" is available in "gif" format from:

<http://arxiv.org/ps/astro-ph/0001500v1>